Strongly correlated electrons and hybrid excitons in a moiré heterostructure

Journal Article

Author(s):
Shimazaki, Yuya; Schwartz, Ido; Watanabe, Kenji; Taniguchi, Takashi; Kroner, Martin (ID); Imamoglu, Atac

Strongly correlated electrons and hybrid excitons in a moiré heterostructure

Yuya Shimazaki*,[1] Ido Schwartz*,[1] Kenji Watanabe,[2] Takashi Taniguchi,[2] Martin Kroner,[1] and Ataç Imamoğlu[1]

[1] *Institute for Quantum Electronics, ETH Zürich, CH-8093 Zürich, Switzerland*
[2] *National Institute for Materials Science, Tsukuba, Ibaraki 305-0044, Japan,*
* These authors contributed equally to this work.

Two dimensional materials and their heterostructures constitute a promising platform to study correlated electronic states[1–5] as well as many body physics of excitons. Here, we present experiments that unite these hitherto separate efforts and show how excitons that are dynamically screened by itinerant electrons to form exciton-polarons[6,7], can be used as a spectroscopic tool to study interaction-induced incompressible states of electrons. We study a $MoSe_2/hBN/MoSe_2$ heterostructure that exhibits a long-period moiré superlattice as evidenced by coherent-hole tunnelling mediated avoided crossings between the intra-layer exciton with three inter-layer exciton resonances separated by $\sim 5\,\mathrm{meV}$. For electron densities corresponding to half-filling of the lowest moiré subband, we observe strong layer pseudospin paramagnetism demonstrated by an abrupt transfer of all ~ 1500 electrons from one $MoSe_2$ layer to the other upon application of a small perpendicular electric field. Remarkably, the electronic state at half-filling of each $MoSe_2$ layer is resilient towards charge redistribution by the applied electric field, demonstrating an incompressible Mott-like state of electrons. Our experiments demonstrate that optical spectroscopy provides a powerful tool for investigating strongly correlated electron physics in the bulk and pave the way for investigating Bose-Fermi mixtures of degenerate electrons and dipolar excitons.

Van der Waals heterostructures incorporating transition metal dichalcogenide (TMD) bilayers open up new avenues for exploring strong correlations using transport and optical spectroscopy. In contrast to similar structures in III-V semiconductors, these heterostructures exhibit possibilities for exotic material combinations, creation of moiré superlattices exhibiting narrow electronic bands[8–11], and strong binding of spatially separated inter-layer excitons[12]. Recently, transport experiments in twisted bilayer graphene demonstrated strongly correlated electron physics in a single system[1–5], ranging from superconductivity to a Mott insulator state as the filling factor ν is varied. In fact, this system realizes a two-dimensional (2D) Fermi-Hubbard model on a triangular lattice with a tunable electron density.

In parallel, optical spectroscopy in van der Waals heterostructures have revealed the prevalence of many-body hybrid light-matter states, termed exciton-polarons[6,7], in the excitation spectra of electron or hole doped monolayers. Advances in material quality and device fab-

rication has lead to the observation of moiré physics of non-interacting excitons in TMD heterobilayers[13–16]. Potential of this new system for many-body physics was recently revealed in demonstration of a long-lived inter-layer exciton condensate[17]. Here, we describe experiments in a heterostructure incorporating a $MoSe_2/hBN/MoSe_2$ homobilayer that in several ways combine the principal developments in these two fields to demonstrate interaction-induced incompressible states of electrons. We provide an unequivocal demonstration of hybridization of inter- and intra-layer excitons by coherent hole tunnelling[11,15,18] between the two $MoSe_2$ layers: the avoided crossings in optical reflection not only show the formation of dipolar excitons with a strong optical coupling but also reveal the existence of moiré bands of inter-layer excitons. We then demonstrate that intra-layer exciton-polaron resonances provide a sensitive tool to investigate correlated electronic states in the bulk. Equipped with this spectroscopic tool, we observe strong layer pseudospin paramagnetism[19,20] and an incompressible Mott-like state of electrons when each layer has half filling.

I. DEVICE STRUCTURE AND BASIC CHARACTERIZATION

Figure 1a shows the schematic of the device structure. By using a double gate structure, we control the electric field E_z and the chemical potential μ of the device independently (see Methods for details). Figure 1b (top panel) is a schematic image of a dipolar exciton formed by coherent coupling of inter-layer exciton (IX) and intra-layer exciton (X) via hole tunnelling. Figure 1b (bottom panel) shows a sketch of electrons in a moiré lattice, probed by intra-layer excitons.

Figure 1c shows a spatial map of total photoluminescence (PL) from the device. Here, both top and bottom gate voltages are at zero Volts. We observe PL from regions with monolayer $MoSe_2$, but not from bilayer $MoSe_2$, where two $MoSe_2$ flakes are in direct contact (the region around the point indicated by the white arrow in Fig. 1c). Contrarily, the $MoSe_2/hBN/MoSe_2$ region shows bright PL. This indicates that the heterostructure becomes a direct band gap system owing to the reduction of the inter-layer hybridization of the valence bands at the Γ point[21], due to the presence of monolayer hBN. Typical PL spectra of the monolayer $MoSe_2$ and the $MoSe_2/hBN/MoSe_2$ region are shown in the inset of Fig. 1c: there are pronounced intra-layer exciton lumi-

nescence peaks in both regions. We observe two distinct exciton peaks in the $MoSe_2/hBN/MoSe_2$ region. This strain-induced energy difference between the PL from the top and bottom layers varies across the sample (see Supplementary Information S2).

II.   COHERENT INTER-LAYER HOLE TUNNELLING AND DIPOLAR EXCITONS

We first analyse the electric field (E_z) dependence of the elementary optical excitations of the $MoSe_2/hBN/MoSe_2$ region in the absence of itinerant electrons or holes. To this end, we scan the top and bottom gate voltages (along L4 indicated in Fig. 3c) together to change E_z while keeping the system in the charge neutral regime. The obtained PL spectrum is depicted in Fig. 2a: using the top (V_{tg}) and bottom (V_{bg}) gate voltage dependence, we determine that the PL spectra around 1.632 eV and 1.640 eV stem from intra-layer exciton in top and bottom layer (X_{top} and X_{bot}), respectively. For high values of $|E_z|$ depicted in the top and bottom parts of the color-coded PL spectrum, we observe PL lines with a strong E_z dependence: we identify these PL lines as originating from inter-layer excitons with a large dipole moment leading to a sizeable Stark shift.

The spectra for positive (negative) V_{tg} regime corresponds to the inter-layer exciton $IX_\uparrow$ ($IX_\downarrow$) which has a hole in the bottom (top) layer and an electron in the top (bottom) layer. The associated dipole-moment of the inter-layer exciton changes its polarity for $V_{tg} \sim 0$. By extrapolating the $IX_\uparrow$ and $IX_\downarrow$ PL lines and finding their crossing point, we estimate the energy difference between the inter- and the intra-layer exciton resonances at $E_z = 0$, which allows us to determine their binding energy difference to be 0.1 ± 0.01 eV.

Figure 2b shows the differential reflectance $(\Delta R/R_0)$ spectrum obtained for the same range of gate voltage scan as that of Fig. 2a. Here, $\Delta R/R_0 \equiv (R - R_0)/R_0$, with R and R_0 denoting the reflectance signal from the $MoSe_2/hBN/MoSe_2$ region, and background reflectance, respectively. In accordance with the PL data (Fig. 2a), we find X_{top} and X_{bot} resonances around 1.632 eV and 1.640 eV, respectively. Moreover, for $V_{tg} \gtrsim 7.5$ V ($V_{tg} \lesssim -7.5$ V), we observe $IX_\uparrow$ ($IX_\downarrow$) hybridizing exclusively with X_{top} (X_{bot}). Figures 2c and 2d show magnified plots of the regions highlighted with blue and green dashed lines in Fig. 2b, confirming avoided crossing of an intra-layer exciton with multiple inter-layer excitons. We first note that the observation of a sizeable reflection signal from $IX_\uparrow$ away from the avoided crossing suggests that it is possible to resonantly excite long-lived inter-layer excitons in these structures. The hybridization of $IX_\uparrow$ lines with X_{top}, together with the lack of an avoided crossing with X_{bot} in Fig. 2c, unequivocally shows that avoided crossings originate exclusively from coherent hole tunnelling schematically shown in Fig. 2e. Our observation, proving that the hole tunnel coupling is much larger

than that of the electron, is consistent with the band alignment expected from first principle band-structure calculations[22]. This conclusion is also confirmed by the data depicted in Fig. 2d, where avoided crossing originates from coherent-hole-tunnelling induced hybridization of $IX_\downarrow$ and X_{bot} schematically shown in Fig. 2f.

One of the most remarkable features of the spectra depicted in Figs. 2c and 2d is the existence of multiple avoided crossings associated with three inter-layer exciton resonances separated in energy by ~ 5 meV. This inter-layer exciton fine-structure demonstrates the existence of a moiré superlattice[8,10,11,13–16], originating from a small twist angle between the two $MoSe_2$ layers (see Methods). The presence of an hBN tunnel barrier strongly suppresses the strength of the associated moiré potential, rendering it sizeable only for the inter-layer excitons[8].

III.   CHARGE CONFIGURATION DETECTION BY EXCITON-POLARON SPECTROSCOPY

The presence of itinerant charges drastically alters the optical excitation spectrum[23]. Recent theoretical and experimental work established that the modified spectrum originates from dynamical screening of excitons by electrons or holes[6,7], leading to the formation of a lower energy attractive polaron (AP) branch. Concurrently, the exciton resonance evolves into a repulsive polaron (RP) (see Supplementary Information S1). The strong sensitivity of the RP resonance energy to changes in electron density renders it an ideal spectroscopic tool for sensing the electron density n in the same layer[24,25]. The strain induced resonance energy difference between X_{top} and X_{bot}, ensuring different energies for the corresponding RP_{top} and RP_{bot}, together with the much weaker sensitivity of RP_{top} (RP_{bot}) on electron density n_b (n_t) in the bottom (top) layer, allows us to determine the charging configuration of the two layers simultaneously. Since we are predominantly interested in the low carrier density regime where the quasi-particle (bare-exciton) weight of the RP resonance is close to unity, we will refer to it as the exciton resonance.

Figures 3a and 3b show the gate voltage dependence of $\Delta R/R_0$ at $E = 1.632$ eV and $E = 1.640$ eV, which correspond to the top (X_{top}) and bottom (X_{bot}) intra-layer exciton resonance energy in the charge neutral regime, respectively. The inset to these figures show a line cut through the dispersive neutral exciton reflection spectrum, indicating the exciton energies at which we monitor $\Delta R/R_0$. Since a small increase of electron density from ~ 0 to 1×10^{11} cm^{-2} results in a change of $\Delta R/R_0$ from ~ -1 to $\gtrsim 0$, the blue regions in Figs. 3a and 3b correspond to the charge neutral regime of each layer. The red and white regions in turn, correspond to the electron or hole doped regime of each layer. This all-optical determination of the charge map of the bilayer provides an invaluable tool for monitoring the bulk properties of 2D

materials.

To enhance the sensitivity of the charge map and to visualize the charge configuration of both layers at the same time, we evaluate and overlay the derivative of $\Delta R/R_0$ ($d(\Delta R/R_0)/dE$) obtained for both layers. The resulting charge map, depicted in Fig. 3c, is closely reminiscent of the charging diagram used to characterize gate-defined quantum dots[26]. The blue regions in Fig. 3c correspond to gate voltages where the charge configuration changes, allowing us to clearly separate the regions (t,b) where the top or bottom layer is neutral (t=i or b=i), electron doped (t=n or b=n) or hole doped (t=p or b=p).

We show typical gate voltage dependence of $\Delta R/R_0$ in Figs. 3d and 3e obtained while scanning the two gates along the lines L1 and L2, indicated in Figs. 3a and 3b, respectively. In both plots, we confirm the emergence of the AP resonance and the associated blue shift of the exciton / RP energy around the charge configuration transition points, confirming the assignment obtained from $d(\Delta R/R_0)/dE$ in Fig. 3c.

Figure 3f shows the gate voltage scan along L3, indicated in Fig. 3c, where we fixed V_{bg} at 4 V and scanned V_{tg}. As we increase the chemical potential by sweeping V_{tg} from negative to positive, we find that initially the bottom layer gets electron doped, since for the chosen V_{bg}, its (single-particle) conduction band energy is lower. For $V_{tg} \simeq 4$ V, electrons are introduced into the top layer as well. In the absence of interactions, we would expect that the electron density in the bottom layer to become independent of further increase of V_{tg}, due to screening of V_{tg} by the free electrons in the top layer. We observe different behavior in Fig. 3f: increasing V_{tg} results in a decrease and eventually total depletion of electrons from the bottom layer. The underlying physics is understood by considering the intra-layer exchange interaction which is maximal if all electrons occupy a single layer. If the ensuing reduction in total repulsive Coulomb energy exceeds the kinetic energy cost of having all electrons in a single layer, layer polarization is favored, leading to the observed depletion of electrons from the bottom layer. This phenomena, termed negative compressibility, was previously observed in transport experiments in bilayer semiconductor systems[27].

IV. INTERACTION INDUCED INCOMPRESSIBLE STATES

The results we present in Sec. II establish the existence of a moiré superlattice for inter-layer excitons. The absence of coherent electron tunnelling on the other hand, indicates that the corresponding electronic moiré subbands in the top and bottom layers do not hybridize. Therefore, our homobilayer realizes a rather unique system exhibiting flat bands with layer and valley-spin degree of freedom. Moreover, negative compressibility (Sec. III) indicates that electron-electron interactions are prominent even at relatively high electron densities

($n \simeq 1 \times 10^{12}\,\mathrm{cm}^{-2}$) where several moiré bands in one layer are occupied. In this section, we explore electron correlation effects by focusing on the low-n regime of the charging map (Fig. 3c) where the (i,i), (i,n), (n,i) and (n,n) regions coalesce. The high sensitivity of the exciton/RP resonance energy, as well as the AP oscillator strength, to changes in electron density once again forms the backbone of our investigation.

Figure 4a shows the gate voltage dependence of $\Delta R/R_0$ at energy of 1.6320 eV. The choice of the energy at which we monitor $\Delta R/R_0$ maximizes the sensitivity to the shift of X_{top} and is indicated by the magenta point in the inset of Fig. 4a. We now choose the horizontal and vertical voltage axes to be $V_E = 0.5V_{tg} - 0.5V_{bg}$ and $V_\mu = (7/15)V_{tg} + (8/15)V_{bg}$. With this choice, vertical (V_μ axis) and horizontal (V_E axis) cuts through the reflectance map leave E_z and μ unchanged, respectively. Remarkably, Fig. 4a shows a periodic modulation of the reflectance as a function of V_μ, particularly in the low n regime. Moreover, the modulation of the X_{top} and X_{bot} reflectance are correlated and symmetric with respect to the $V_E = -1$ V axis (see Supplementary Fig. S4), indicating that for this value of V_E, the conduction band edge energy of the two layers is aligned.

To gain further insight, we first determine the repulsive polaron resonance energy ($E_{X_{top}}$) by fitting the reflectance spectrum with a dispersive Lorentzian lineshape (see Supplementary Information S3) and then plot the derivative of $E_{X_{top}}$ with respect to V_μ in Fig. 4b. The resulting map shows a remarkable checkerboard pattern that is complementary for the top and bottom layers (see Supplementary Fig. S4). Since the blue shift of X_{top} (X_{bot}) resonance while increasing V_μ corresponds to filling of electrons in the top (bottom) layer, the complementary checkerboard patterns in Figs. 4b and S4f indicates a layer-by-layer filling of electrons[28].

The observed periodicity in Fig. 4 indicates the existence of moiré subbands for electrons. In anticipation of the subsequent discussion, we define a layer filling factor ν_L (L = "top" or "bot" indicating top or bottom layer) such that $\nu_L = 1/2$ corresponds to 1 electron per moiré unit cell of a single layer, and a total filling factor ν as $\nu = \nu_{top} + \nu_{bot}$. From a capacitive model of our device, we determine that $\nu = 1/2$ coincides with electron density of $n = 2 \times 10^{11}\mathrm{cm}^{-2}$. At this low electron density, r_s parameter, which describes the ratio of interaction energy to kinetic energy, is estimated to be $r_s \gtrsim 14$. The density periodicity corresponds to a moiré superlattice latice constant of $\lambda_{moiré} = 24$ nm by assuming a triangular superlattice (see Methods for the estimation of r_s and $\lambda_{moiré}$). We indicate the values of ν corresponding to $\nu = 1/2, 1, 3/2, 2$ with blue dashed lines in Fig. 4b. We confirmed that the same periodicity also appears in the AP photoluminescence intensity (see Figs. S4g and S4h).

Figures 5a and 5b show the V_E dependence of $\Delta R/R_0$ for fixed V_μ for $\nu = 1/2$ and $\nu = 1$, respectively. In Fig. 5a, we find an abrupt shift of exciton energy to-

gether with complete oscillator strength transfer between AP_{top} and AP_{bot}, demonstrating that the electrons are completely transferred from one layer to the other. Figures 5c and 5e show the extracted X_{bot} and X_{top} energies around $\nu = 1/2$. Remarkably, the abrupt jump in excitonic resonance is pronounced at $\nu = 1/2$, and smeared out for both lower ($\nu = 0.35$) and higher filling factors ($\nu = 0.65$). These measurements show that abrupt transfer of practically all of the ~ 1500 electrons within the region we monitor optically is linked to the emergence of an interaction-induced incompressible state in the lowest moiré subband at $\nu = 1/2$ filling. As the filling factor is increased (decreased) towards $\nu = 1/2$, the electronic system shows an ever stronger layer pseudospin paramagnetism, due to the enhanced role of interactions, but otherwise exhibits a continuous inter-layer transfer of electrons as a function of E_z that would be expected from a compressible state. Close to $\nu = 1/2$, there is a phase transition to an incompressible state that can be accommodated either in the top or bottom layer (see Fig. 5g). Remarkably, inter-layer charge transfer takes place upon changing V_E by only $1.9\,\text{mV}$: the corresponding change in the single particle energy detuning between the top and bottom layers ($26\,\mu\text{eV}$) is much smaller than $k_{\text{B}}T$ ($360\,\mu\text{eV}$) (see Supplementary Information S5).

Figure 5b shows that for $\nu = 1$, $\Delta R/R_0$ is characterized by 3 plateau-like regions. We attribute the abrupt jumps in the excitonic resonance energy to the transition from $(\nu_{\text{top}}, \nu_{\text{bot}}) = (0, 1)$, through $(1/2, 1/2)$, to $(1, 0)$ configurations (see Fig. 5h). This explanation is confirmed by the corresponding changes in the oscillator strength of the AP resonances of the top and bottom layers. In $(1, 0)$ and $(0, 1)$ configurations, we measure a reflectance signal either from AP_{top} or AP_{bot}, consistent with full layer polarization. In the $(1/2, 1/2)$ configuration, we find the oscillator strength of AP_{top} and AP_{bot} to be identical and equal to half the value obtained under $(1,0)$ for AP_{top}. The extracted excitonic resonance energy X_{bot} and X_{top} around $\nu = 1$ is shown in Figs. 5d and 5f, respectively. The plateau structure of the $(1/2, 1/2)$ state with abrupt changes of electron density difference between the layers at $V_E = -1.3\,\text{V}$ and $V_E = -0.5\,\text{V}$ is clearly visible at $\nu = 1$, but is smeared out for both lower ($\nu = 0.85$) and higher fillings ($\nu = 1.15$). The emergence of the stabilized $(1/2, 1/2)$ plateau at $\nu = 1$ strongly suggests that there is mutual stabilization of the incompressible electronic state due to the inter-layer electron-electron interactions. The energy gap of the incompressible $(1/2, 1/2)$ state is estimated to be $5.5\,\text{meV}$ (see Supplementary Information S6). The reflectance data for higher fillings ($\nu = 3/2$ and $\nu = 2$) are shown in the supplementary Information (Fig. S5): in stark contrast to the $(1/2, 1/2)$ configuration at $\nu = 1$, a plateau at the $(1, 1)$ electron configuration is missing at $\nu = 2$ filling, indicating that the state with the corresponding integer fillings is not sufficiently stabilized by the inter-layer interactions.

Finally, we also perform the measurement under a perpendicular magnetic field $B_z = 7\,\text{T}$ (see Supplementary Information). In Fig. S6, we find that the plateau structure observed for $\nu = 2$ under full valley polarization of electrons is identical to that observed for $B_z = 0\,\text{T}$, although the total number of electronic states per moiré subband is halved due to giant valley-spin susceptibility of electrons in $MoSe_2$[24]. This observation shows that the incompressibility is determined by filling of each moiré site by a single electron, irrespective of its (valley) degeneracy. The observation supports that our identification of $n = 2 \times 10^{11}\,\text{cm}^{-2}$ yielding half-filling of a single-layer moiré subband. We also find that the reflectance spectrum does not show any valley polarization at $B_z = 7\,\text{T}$ for $\nu \lesssim 1/2$ state; However, the resilience against valley polarization is not sufficient to claim anti-ferromagnetic order.

V. DISCUSSION

The experiments we describe in Sec. IV demonstrate the existence of Mott-like incompressible electronic states for half-filling of the lowest moiré subband. Unlike prior reports[13–16], our experiments are carried out for long moiré superlattice latice constant of $\lambda_{\text{moiré}} = 24\,\text{nm}$ and r_s parameter of $r_s \gtrsim 14$. The weakness of the moiré potential stemming from the hBN layer separating the two $MoSe_2$ layers in turn ensures that the on-site interaction strength is larger than the depth of the moiré potential. In this sense, the homobilayer system realizes a rather unique regime that goes beyond the standard Fermi-Hubbard model.

In addition to establishing twisted TMD homobilayers as a promising system for investigating Mott-Wigner physics[10,29–31] originating from strong electronic correlations, our experiments open up new avenues for exploring interactions between dipolar excitons and electrons confined to flat bands. In particular, the structure we analysed could be used to realize and study Bose-Fermi mixtures consisting of degenerate electrons strongly interacting with an exciton condensate generated by resonant laser excitation. The phase diagram of such a mixture is not fully understood[32] but is expected to provide a rich playground for many-body physics[33].

[1] Cao, Y. *et al.* Unconventional superconductivity in magic-angle graphene superlattices. *Nature* **556**, 43–50 (2018).

[2] Yankowitz, M. *et al.* Tuning superconductivity in twisted bilayer graphene. *Science* **363**, 1059–1064 (2019).

[3] Liu, X. *et al.* Spin-polarized Correlated Insulator and Superconductor in Twisted Double Bilayer Graphene Preprint at http://arxiv.org/abs/1903.08130 (2019).

[4] Sharpe, A. L. *et al.* Emergent ferromagnetism near three-quarters filling in twisted bilayer graphene. *Science* **365**, 605–608 (2019).

[5] Lu, X. *et al.* Superconductors, orbital magnets and correlated states in magic-angle bilayer graphene. *Nature* **574**, 653–657 (2019).

[6] Sidler, M. *et al.* Fermi polaron-polaritons in charge-tunable atomically thin semiconductors. *Nature Physics* **13**, 255–261 (2017).

[7] Efimkin, D. K. & MacDonald, A. H. Many-body theory of trion absorption features in two-dimensional semiconductors. *Physical Review B* **95**, 035417 (2017).

[8] Yu, H., Liu, G.-B., Tang, J., Xu, X. & Yao, W. Moiré excitons: From programmable quantum emitter arrays to spin-orbit–coupled artificial lattices. *Science Advances* **3**, e1701696 (2017).

[9] Wu, F., Lovorn, T. & MacDonald, A. Topological Exciton Bands in Moiré Heterojunctions. *Physical Review Letters* **118**, 147401 (2017).

[10] Wu, F., Lovorn, T., Tutuc, E. & MacDonald, A. H. Hubbard Model Physics in Transition Metal Dichalcogenide Moiré Bands. *Physical Review Letters* **121**, 026402 (2018).

[11] Ruiz-Tijerina, D. A. & Fal'ko, V. I. Interlayer hybridization and moiré superlattice minibands for electrons and excitons in heterobilayers of transition-metal dichalcogenides. *Physical Review B* **99**, 125424 (2019).

[12] Rivera, P. *et al.* Interlayer valley excitons in heterobilayers of transition metal dichalcogenides. *Nature Nanotechnology* **13**, 1004–1015 (2018).

[13] Seyler, K. L. *et al.* Signatures of moiré-trapped valley excitons in MoSe$_2$/WSe$_2$ heterobilayers. *Nature* **567**, 66–70 (2019).

[14] Tran, K. *et al.* Evidence for moiré excitons in van der Waals heterostructures. *Nature* **567**, 71–75 (2019).

[15] Alexeev, E. M. *et al.* Resonantly hybridized excitons in moiré superlattices in van der Waals heterostructures. *Nature* **567**, 81–86 (2019).

[16] Jin, C. *et al.* Observation of moiré excitons in WSe$_2$/WS$_2$ heterostructure superlattices. *Nature* **567**, 76–80 (2019).

[17] Wang, Z. *et al.* Evidence of high-temperature exciton condensation in two-dimensional atomic double layers. *Nature* **574**, 76–80 (2019).

[18] Gerber, I. C. *et al.* Interlayer excitons in bilayer MoS$_2$ with strong oscillator strength up to room temperature. *Physical Review B* **99**, 035443 (2019).

[19] Zheng, L., Ortalano, M. W. & Das Sarma, S. Exchange instabilities in semiconductor double-quantum-well systems. *Physical Review B* **55**, 4506–4515 (1997).

[20] Ezawa, Z. F. *Quantum Hall Effects: Field Theoretical Approach and Related Topics* (World Scientific, 2000).

[21] Zhang, Y. *et al.* Direct observation of the transition from indirect to direct bandgap in atomically thin epitaxial MoSe$_2$. *Nature Nanotechnology* **9**, 111–115 (2014).

[22] Özçelik, V. O., Azadani, J. G., Yang, C., Koester, S. J. & Low, T. Band alignment of two-dimensional semiconductors for designing heterostructures with momentum space matching. *Physical Review B* **94**, 035125 (2016).

[23] Xu, X., Yao, W., Xiao, D. & Heinz, T. F. Spin and pseudospins in layered transition metal dichalcogenides. *Nature Physics* **10**, 343–350 (2014).

[24] Back, P. *et al.* Giant Paramagnetism-Induced Valley Polarization of Electrons in Charge-Tunable Monolayer MoSe$_2$. *Physical Review Letters* **118**, 237404 (2017).

[25] Smoleński, T. *et al.* Interaction-Induced Shubnikov–de Haas Oscillations in Optical Conductivity of Monolayer MoSe$_2$. *Physical Review Letters* **123**, 097403 (2019).

[26] Hanson, R., Kouwenhoven, L. P., Petta, J. R., Tarucha, S. & Vandersypen, L. M. K. Spins in few-electron quantum dots. *Reviews of Modern Physics* **79**, 1217–1265 (2007).

[27] Eisenstein, J. P., Pfeiffer, L. N. & West, K. W. Compressibility of the two-dimensional electron gas: Measurements of the zero-field exchange energy and fractional quantum Hall gap. *Physical Review B* **50**, 1760–1778 (1994).

[28] Hunt, B. M. *et al.* Direct measurement of discrete valley and orbital quantum numbers in bilayer graphene. *Nature Communications* **8**, 948 (2017).

[29] Imada, M., Fujimori, A. & Tokura, Y. Metal-insulator transitions. *Reviews of Modern Physics* **70**, 1039–1263 (1998).

[30] Camjayi, A., Haule, K., Dobrosavljević, V. & Kotliar, G. Coulomb correlations and the Wigner–Mott transition. *Nature Physics* **4**, 932–935 (2008).

[31] Zarenia, M., Neilson, D. & Peeters, F. M. Inhomogeneous phases in coupled electron-hole bilayer graphene sheets: Charge Density Waves and Coupled Wigner Crystals. *Scientific Reports* **7**, 11510 (2017).

[32] Ludwig, D., Floerchinger, S., Moroz, S. & Wetterich, C. Quantum phase transition in Bose-Fermi mixtures. *Physical Review A* **84**, 033629 (2011).

[33] Laussy, F. P., Kavokin, A. V. & Shelykh, I. A. Exciton-Polariton Mediated Superconductivity. *Physical Review Letters* **104**, 106402 (2010).

ACKNOWLEDGMENTS

AUTHOR CONTRIBUTIONS

COMPETING INTERESTS

ADDITIONAL INFORMATION
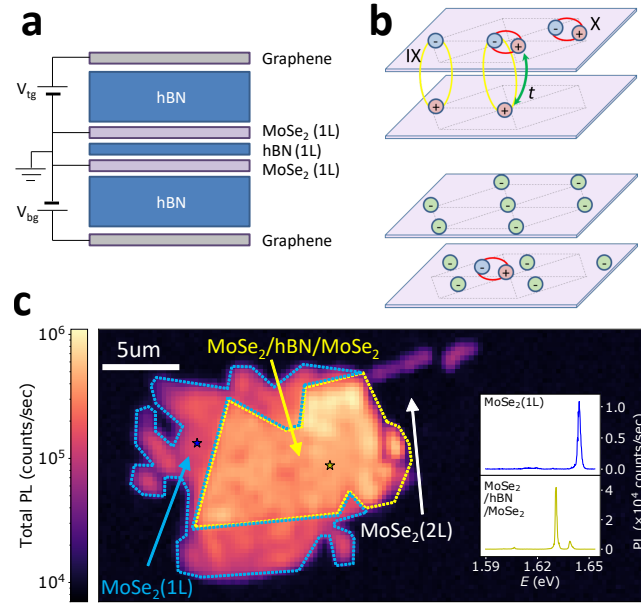
Figure 1. Device structure and basic characterization. a Schematic image of the device structure. V_{tg} (V_{bg}) is the applied voltage to the top (bottom) gate. **b** Schematic image of coupled inter- and intra-layer exciton (top panel) and electrons in a moiré lattice probed by the intra-layer exciton (bottom panel). Purple planes correspond to $MoSe_2$ layers, and dashed lines indicate a moiré unit cell. The pink (light blue) circles with $+$ ($-$) sign indicate holes (electrons) forming excitons, and the electron-hole pair enclosed by the red (yellow) ellipse indicates intra-layer (inter-layer) exciton. The green double arrow in the top panel indicates tunnel coupling of holes through a monolayer hBN barrier. The light green circles in the bottom panel indicate electrons filling the moiré lattice. **c** Spatial map of integrated photoluminescence from $1.59\,eV$ to $1.65\,eV$. The blue and yellow dashed lines indicate the boundary of the monolayer $MoSe_2$ and $MoSe_2/hBN/MoSe_2$ regions, respectively. The inset shows representative PL spectra of monolayer $MoSe_2$ and $MoSe_2/hBN/MoSe_2$ measured at the positions indicated with the blue and yellow stars in the main figure, respectively.
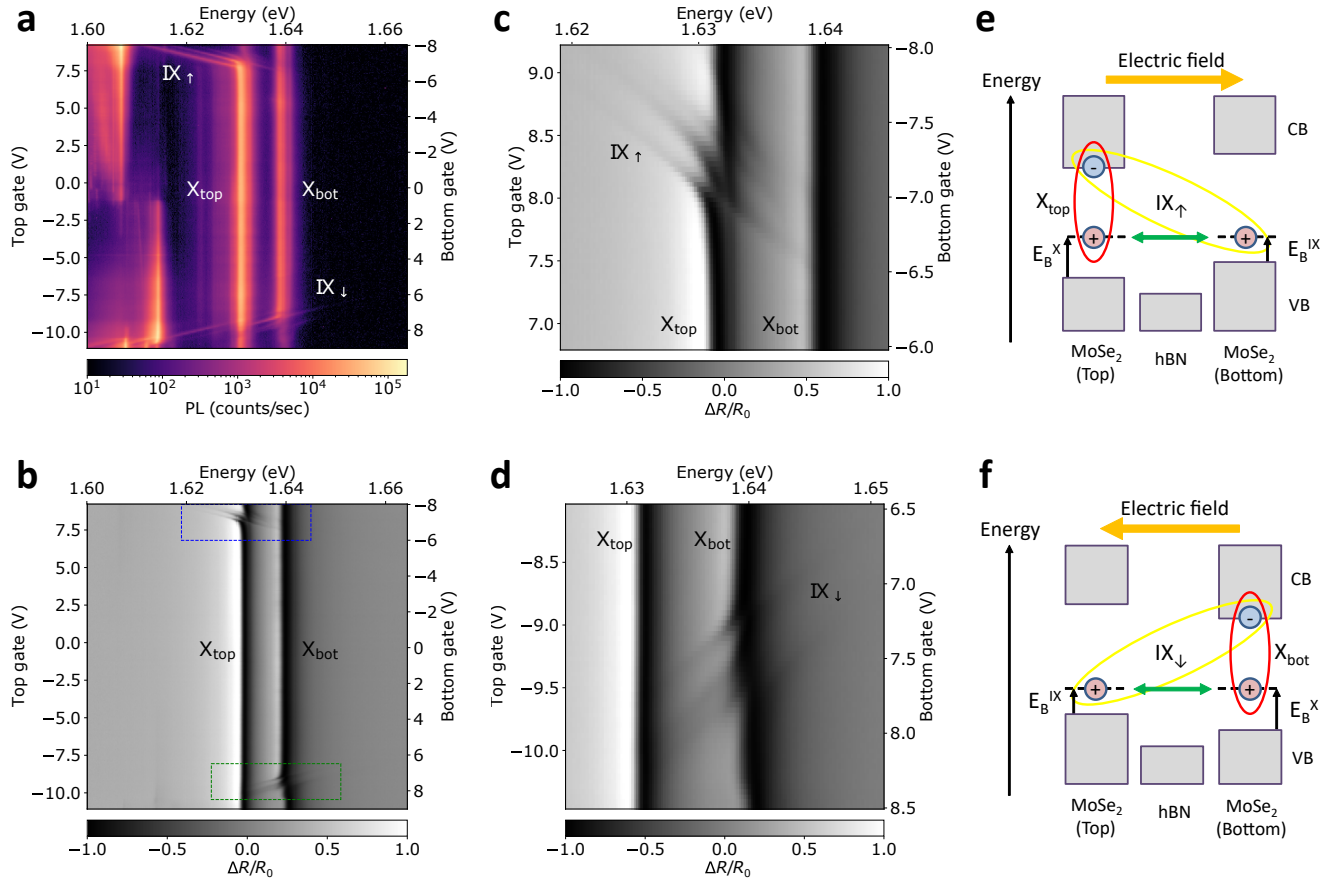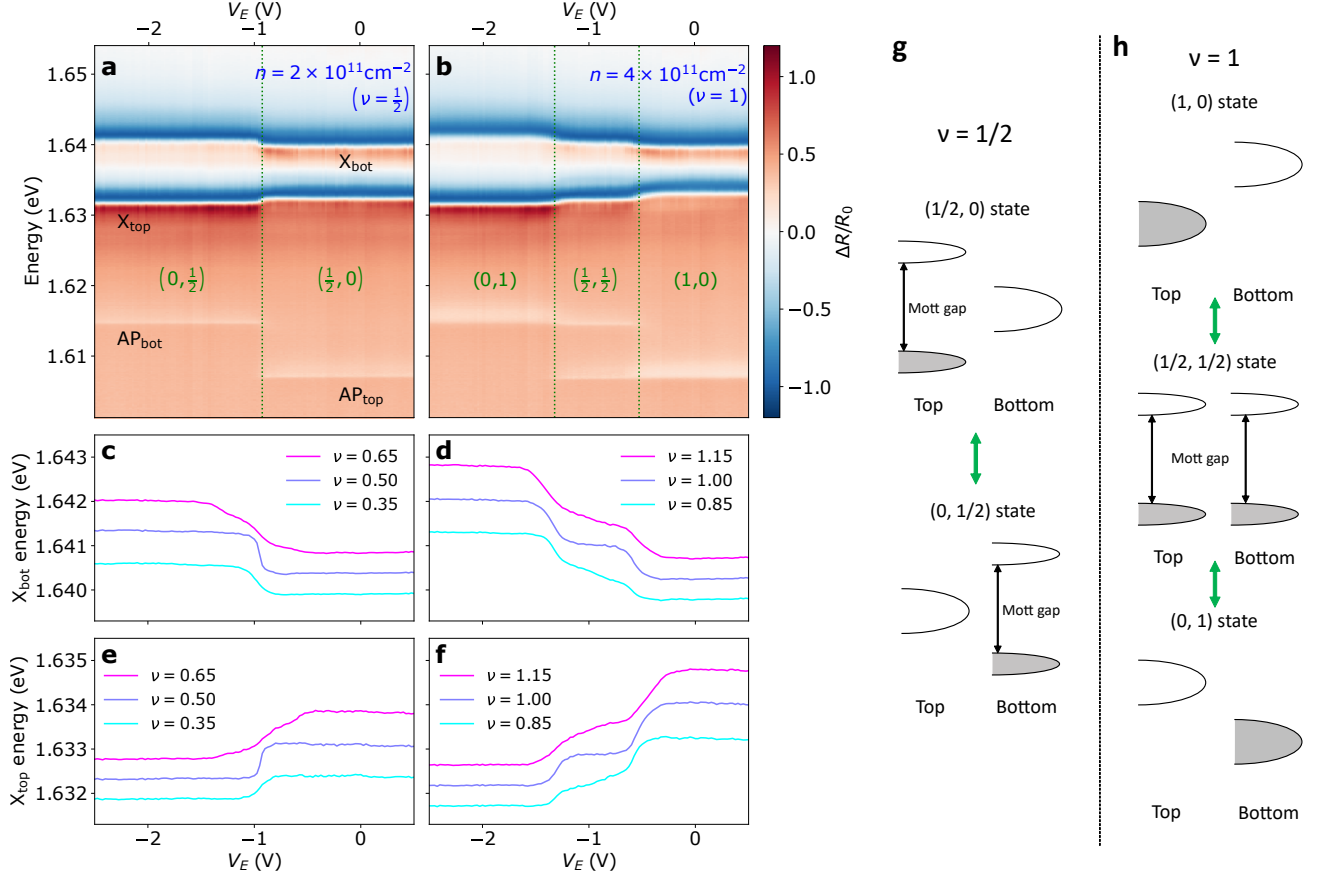
Figure 2. Electric field dependence of photoluminescence and differential reflectance at charge neutrality. Gate dependence of photoluminescence **a** and differential reflectance **b** of MoSe$_2$/hBN/MoSe$_2$. Top and bottom gate voltages are scanned together to tune the electric field at a constant chemical potential (scanned along the dashed line L4 shown in Fig. 3c). The intensity of the photoluminescnece in **a** is shown in log scale. **c**, **d** Magnified plots of **b**. The corresponding region of **c** and **d** is indicated by the blue and green dashed rectangles in **b**, respectively. **e**, **f** Schematic of the energy bands and the exciton energy alignment under electric fields where the excitons are in resonance. Green double arrows represent hole tunnelling.
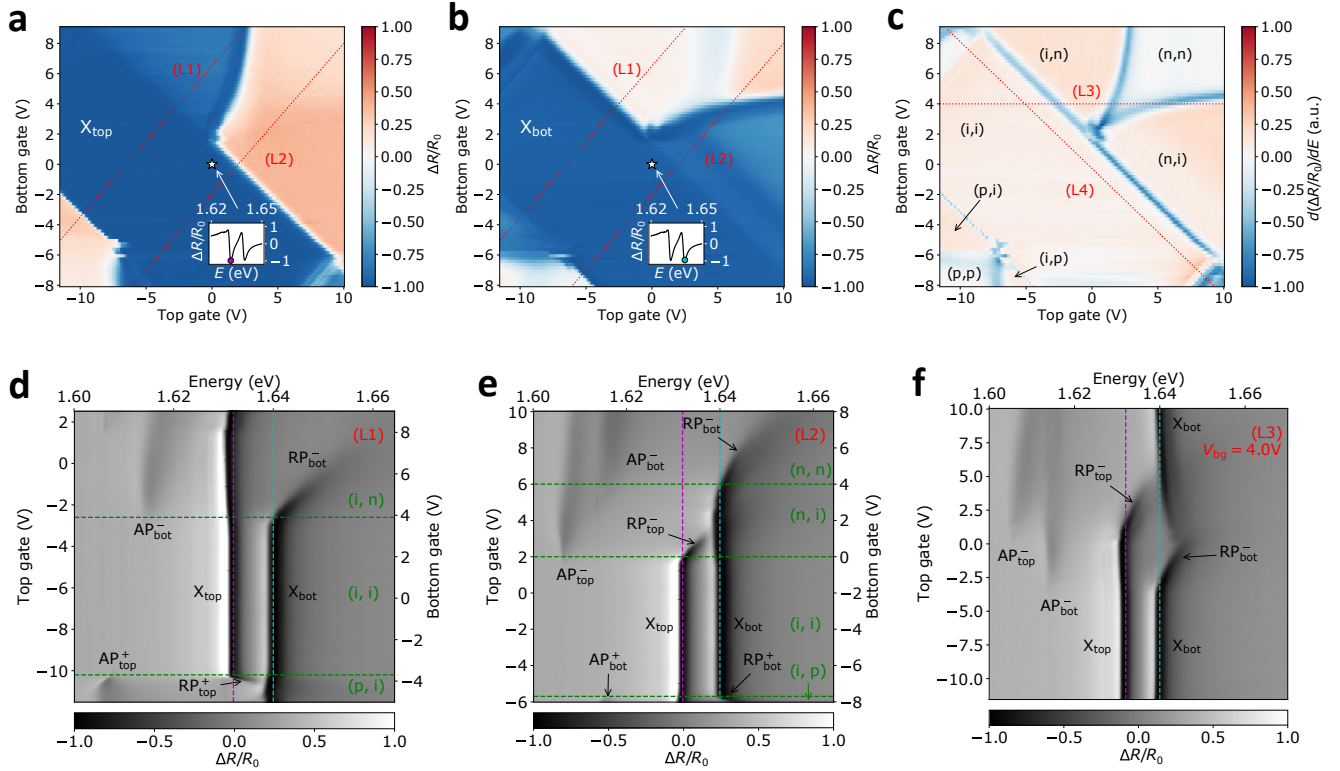
Figure 3. Gate dependence of differential reflectance spectrum of MoSe₂/hBN/MoSe₂. a, b Two gates dependence maps of differential reflectance around top (**a**) and bottom (**b**) intra-layer exciton resonances ($E = 1.632$eV and $E = 1.640$eV, respectively). The insets of **a** and **b** show the differential reflectance spectrum at $(V_{tg}, V_{bg}) = (0V, 0V)$ (indicated with the white stars in the maps). The magenta and cyan dots in the insets indicate the points where $E = 1.632$eV and $E = 1.640$eV, respectively. **c** Charge configuration diagram obtained by derivative of the differential reflectance spectrum with respect to energy (sum of the derivatives at $E = 1.632$eV and $E = 1.640$eV). The charge configuration for each layer is indicated by p, i, n which correspond to hole doped (p), neutral (i), electron doped (n), and shown in the order of (top, bottom). **d - f** Gate dependence of differential reflectance along the dashed lines L1 (**d**), L2 (**e**), and L3 (**f**) shown in **a**, **b** and **c**. Magenta and cyan dashed lines indicate the top ($E = 1.632$eV) and bottom ($E = 1.640$eV) exciton resonance energies, respectively. AP_L^C and RP_L^C stand for intra-layer attractive and repulsive polarons, where L = "top" or "bot" stands for top or bottom layer, and C = + or − stands for hole or electron as Fermi sea carriers. Charge configuration is written in green together with the green dashed lines indicating the charge configuration transition point.
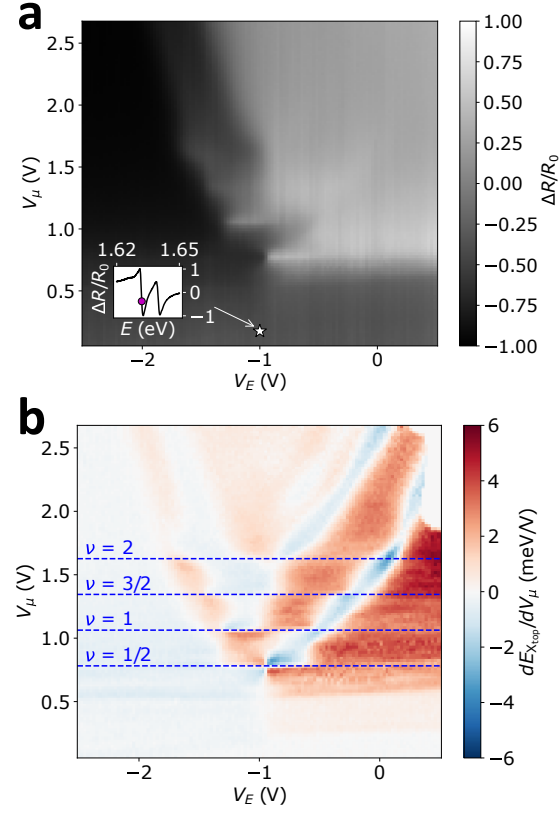
Figure 4. Gate dependence of intra-layer exciton resonance in low electron density regime. a Gate dependence map of differential reflectance around top intra-layer exciton resonance ($E = 1.6320\text{eV}$). The inset of **a** shows the differential reflectance spectrum at $(V_E, V_\mu) = (-1\text{V}, 0.175\text{V})$ (indicated with the white star in the map). **b** Gate dependence map of top intra-layer exciton resonance energy differentiated by V_μ.

Figure 5. Electric field dependence of differential reflectance spectrum in low electron density regime. a, b Electric field (V_E) dependence of differential reflectance spectrum for fixed V_μ at $\nu = 1/2$ and $\nu = 1$. The charge configuration of top and bottom layer is indicated by $(\nu_{\text{top}}, \nu_{\text{bot}})$ in green. **c, d** V_E dependence of X_{bot} resonance energy around total filling of $\nu = 1/2$ (**c**) and $\nu = 1$ (**d**). **e, f** V_E dependence of X_{top} resonance energy around total filling of $\nu = 1/2$ (**e**) and $\nu = 1$ (**f**). In **c** - **f**, the cyan curves are without offset and other curves are displaced by $0.5\,\text{meV}$ (purple) and $1.0\,\text{meV}$ (magenta). **g, h** Schematic picture of the charge configuration with density of states at filling of $\nu = 1/2$ (**g**) and $\nu = 1$ (**h**).

METHODS

A. Device fabrication

The device structure is shown in Extended data Figure 1. All MoSe$_2$, graphene, and hBN flakes are obtained by mechanical exfoliation of bulk crystals. The flakes are assembled together using the dry transfer technique[34] in an Ar filled glove box. The crystal axis of top and bottom MoSe$_2$ layers are aligned to be close to 0 degree using tear-and-stack technique[35]. We expect to have the effect of moiré potential from a small twist angle of MoSe$_2$ layers, but not between MoSe$_2$ and hBN layers due to the large lattice constant mismatch ($a_{\mathrm{MoSe_2}} = 3.32\,\text{Å}$(ref.[22]) and $a_{\mathrm{hBN}} = 2.51\,\text{Å}$(ref.[36])). The metal electrodes to graphene layers are formed by Ti/Au ($5\,\mathrm{nm}/145\,\mathrm{nm}$). The contact to the bottom graphene gate is formed by Cr/Au ($3\,\mathrm{nm}/147\,\mathrm{nm}$) using the one-dimensional contact technique[34] by etching the hBN layer with reactive ion etching using $\mathrm{CHF_3/O_2}$ as mixture gas.

B. Optical spectroscopy

The photoluminescence measurements were performed using a HeNe laser (633nm) as an excitation source. The reflectance measurements were performed using a single mode fiber coupled broadband LED with a center wavelength of 760nm and a bandwidth of 20nm. In both photoluminescence and reflectance measurements, we used a long working distance apochromatic objective lens with NA = 0.65 (attocube LT-APO/LWD/VISIR/0.65). All optical spectroscopy measurements have been performed at cryogenic temperature ($T \sim 4\mathrm{K}$). All data in the main text is obtained at zero magnetic field $B_z = 0$ T.

C. Capacitance parameters

Thickness of top and bottom hBN layers are estimated to be $63.3\,\mathrm{nm}$ and $52.7\,\mathrm{nm}$ from white light reflectance spectrum. As a dielectric constant of hBN, we used 3.7 (ref.[37]). We expect the uncertainty to be about 10% for both hBN thickness and dielectric constant, which gives around 14% of error in the calculation of carrier density.

D. Estimation of r_s parameter and moiré periodicity from electron density

The r_s parameter (Wigner-Seitz radius divided by the effective Bohr radius) that describes the ratio between kinetic energy to Coulomb energy is given by $r_s = 1/a_{\mathrm{B}}^*\sqrt{\pi n}$ (ref.[19]). Here, $a_{\mathrm{B}}^* = 4\pi\varepsilon\varepsilon_0\hbar^2/m_e^*e^2 = 0.91\,\mathrm{nm}$ is the effective Bohr radius in an encapsulated MoSe$_2$ monolayer, m_e^* is the effective electron mass and $\varepsilon = (\varepsilon_{\parallel,\mathrm{MoSe_2}} + \varepsilon_{\parallel,\mathrm{hBN}})/2$ is the lattice dielectric constant[19].

For the calculation we used $m_e^* = 0.7m_e$ (ref.[38]), where m_e is the bare electron mass and the in-plane dielectric constants $\varepsilon_{\parallel,\mathrm{MoSe_2}} = 17.1$ and $\varepsilon_{\parallel,\mathrm{hBN}} = 6.93$ (ref.[37]). For electron density of $n = 2 \times 10^{11}\,\mathrm{cm^{-2}}$ ($\nu = 1/2$) we get $r_s \simeq 14$ and it is reduced to $r_s \simeq 7$ at density of $n = 8 \times 10^{11}\,\mathrm{cm^{-2}}$ ($\nu = 2$). We emphasize that the above values for the r_s parameter are underestimated. At these low densities the inter-electron separation, $r_0 = 1/\sqrt{n\pi} > 10\,\mathrm{nm}$, is much larger than the MoSe$_2$ layer thickness $d_{\mathrm{MoSe_2}} \approx 0.7\,\mathrm{nm}$. In this limit[39], the screening of the interactions is dominated by the hBN dielectric, therefore a better approximation is to take the dielectric constant to be $\varepsilon = \varepsilon_{\parallel,\mathrm{hBN}}$, that results in $r_s \simeq 24$ for electron density of $n = 2 \times 10^{11}\,\mathrm{cm^{-2}}$ ($\nu = 1/2$) and $r_s \simeq 12$ for $n = 8 \times 10^{11}\,\mathrm{cm^{-2}}$ ($\nu = 2$).

The moiré superlattice lattice constant $\lambda_{\mathrm{moiré}}$ is estimated from the following relation by assuming a triangular moiré superlattice: $A_{\mathrm{moiré}} = (\sqrt{3}/2)\lambda_{\mathrm{moiré}}^2 = 1/n_{\mathrm{moiré}}$, where $A_{\mathrm{moiré}}$ is the moiré superlattice unit cell area and $n_{\mathrm{moiré}}$ is the electron density that corresponds to one electron occupation per moiré superlattice unit cell. We used $n_{\mathrm{moiré}} = 2 \times 10^{11}\,\mathrm{cm^{-2}}$ which is obtained from the periodicity of the differential reflectance modulation as we discussed in the main text, that gives $\lambda_{\mathrm{moiré}} \sim 24\,\mathrm{nm}$. The twist angle θ between MoSe$_2$ layers is then estimated to be $\theta = 0.8°$ using the following relation: $\lambda_{\mathrm{moiré}} = a_{\mathrm{MoSe_2}}/\theta$, where $a_{\mathrm{MoSe_2}} = 3.32\,\text{Å}$ is the lattice constant of MoSe$_2$ (ref.[22]).

E. Verification of moiré periodicity estimation using inter-layer exciton fine structure analysis

Here, we estimate the moiré periodicity from the fine structure energy scale of inter-layer exciton. In the limit when the moiré potential is weak compared to the kinetic energy scale, umklapp scattering by moiré potential is the dominant origin of the fine structure of inter-layer exciton. In this limit, the energy difference of the two lowest energy inter-layer excitons is approximately described by the kinetic energy of the inter-layer exciton at the momentum $q_{\mathrm{moiré}} = 4\pi/(\sqrt{3}\lambda_{\mathrm{moiré}})$, where $\lambda_{\mathrm{moiré}}$ is moiré periodicity[9,11]. Using the energy splitting of the first and second lowest energy inter-layer exciton $\Delta E_{1,2}$, $\lambda_{\mathrm{moiré}}$ is obtained using

$$\Delta E_{1,2} \sim \frac{\hbar^2 q_{\mathrm{moiré}}^2}{2M} \qquad (1)$$

$$\lambda_{\mathrm{moiré}} \sim \frac{2h}{\sqrt{6M\Delta E_{1,2}}} \qquad (2)$$

where the total mass of exciton is $M = m_e^* + m_h^* = 1.3m_e$ ($m_e^* = 0.7m_e$ from ref.[38] and $m_h^* = 0.6m_e$ from ref.[21]). From Fig. 2c in the main text, the energy splitting is $\Delta E_{1,2} \sim 4.4\,\mathrm{meV}$, which corresponds to $\lambda_{\mathrm{moiré}} \sim 19\,\mathrm{nm}$. At a different spot, from Fig. S3d in the supplementary information, the energy splitting is $\Delta E_{1,2} \sim 3.7\,\mathrm{meV}$, which corresponds to $\lambda_{\mathrm{moiré}} \sim 20\,\mathrm{nm}$. Both values are

qualitatively similar to what we obtained from the density periodicity of the reflectance signal ($\lambda_{\text{moiré}} \sim 24$ nm from Fig. 4b and $\lambda_{\text{moiré}} \sim 25$ nm from Fig. S10). We note that the third lowest energy inter-layer exciton line observed in reflectance is not captured well by this simple model. In reality, the energy spacing of the inter-layer excitons depends on the magnitude of moiré potential, and the analysis we present here could only yield a rather rough estimate of the moiré periodicity.

F. Effect of strain on moiré periodicity

Moiré superlattice emerges from a twist angle, lattice constant difference, or a combination of the two. In the main text, we attributed our superlattice to be originating from this twist angle. Here we discuss how much strain induced lattice constant modification changes the moiré periodicity. Moiré periodicity for twist angle of θ and lattice constant difference ratio of two layers δ (ref.[40]), which corresponds to strain difference of two layers, is expressed as:

$$\lambda_{\text{moiré}} = \frac{a_{\text{MoSe}_2}(1+\delta)}{\sqrt{2(1+\delta)(1-\cos\theta) + \delta^2}} \quad (3)$$

Extended Data Figure 2a plots the relation of biaxial strain difference (δ) and twist angle (θ) for fixed $\lambda_{\text{moiré}}$ using Eq. 3 ($a_{\text{MoSe}_2} = 3.32$ Å). In the main text, we have shown that there is intra-layer exciton energy difference between top and bottom layers, which is about 8 meV. By assuming this is due to strain difference, the amount of strain difference is on the order of 0.1 ~ 0.25 %. We base our rough estimate on values reported in literature: uniaxial strain MoS_2: 70 meV/% (ref.[41]), 45 meV/% (ref.[42]), 48 meV/% (ref.[43]), biaxial strain MoSe_2: 33 meV/% (ref.[44]). For $\lambda_{\text{moiré}} \sim 24$ nm, the moiré periodicity within this strain range is dominated by twist angle, and hardly modified by strain (only 1.4 % reduction of $\lambda_{\text{moiré}}$ for 0.25 % strain assuming fixed twist angle of $0.8°$ as we show in Extended Data Figure 2b). On the other hand, to introduce a moiré periodicity of ~ 24 nm only with strain difference, more than 1.3 % of strain difference is required, which is unlikely from the magnitude of the energy splitting of intra-layer excitons. The spectrum at another spot which we show in Supplementary Information S2, exhibits 5 meV energy splitting of top and bottom layer intra-layer excitons. From this energy difference, the amount of strain difference is estimated to be in the order of 0.07 ~ 0.15 %, which results in only 0.5 % of $\lambda_{\text{moiré}}$ reduction, assuming fixed twist angle of $0.8°$.

G. First principle calculation of the tunnel coupling and the moiré potential

We perform density functional theory (DFT) calculations using Quantum ESPRESSO[45]. We use pro-jector augmented wave (PAW) pseudopotentials with generalized gradient approximation (GGA) (Perdew-Burke-Ernzerhof (PBE) functional) from PSlibrary 1.0.0 (ref.[46]). To reduce computation cost, we neglect spin-orbit interaction and used non-relativistic pseudopotentials. Computations are performed with 48 cores on a high-performance computing cluster.

We take lattice structure parameters for MoSe_2 from ref.[47], which gives a lattice constant $a_{\text{MoSe}_2} = 3.32$ Å. The lattice constant of hBN given in ref.[36] is $a_{\text{hBN}} = 2.504$ Å. We uniformly stretched the hBN lattice by -0.56 % and set the lattice constant of hBN as $a_{\text{hBN}}^{\text{stretch}} = 2.49$ Å to form 3×3 MoSe_2 and 4×4 hBN commensurate supercell. We take the interlayer distance of MoSe_2 and hBN from ref.[48], and set the thickness of vacuum layer between MoSe_2 and hBN as $d_{\text{Se}-\text{hBN}} = 3.36$ Å. We use a plane-wave cutoff energy of 60 Ry and charge density cutoff energy of 480 Ry. The Brillouin zone is sampled with $9 \times 9 \times 1$ k-point grid. We use a slab geometry with a 30 Å thick vacuum layer.

Extended Data Figures 3a to 3c show the actual R-stacked (0 degree twist angle) $\text{MoSe}_2/\text{hBN}/\text{MoSe}_2$ supercell for different lattice displacement configurations which we use for the calculation. $\alpha = \text{h}, \text{X}, \text{M}$ denote hexagon center, chalcogen, and metal site of TMDs, and $\text{R}_{\text{h}}^{\alpha}$ denotes the specific lattice displacement for R-stacking where α site of top MoSe_2 is aligned with h site of bottom MoSe_2. Extended Data Figures 3d to 3f show the calculated band structure shown with mini-Brillouin zone. We take the vacuum level as energy reference (0 eV). Due to zone folding, the K and K' points of MoSe_2 come to the γ point of the mini-Brillouin zone (the K point of hBN comes to the κ point of the mini-Brillouin zone). Therefore, the lowest conduction bands and the highest valence bands at the γ point are the ones from MoSe_2. Since the inter-layer hybridization effect is substantially smaller than directly contacting TMD heterostructure[8–10], these band structures look almost the same except for a slightly visible energy splitting of $\text{R}_{\text{h}}^{\text{h}}$ displacement. Though the energy modulation is substantially smaller, the calculation shows about 0.5 meV modulation for the lowest conduction band, and 5 meV modulation for the highest valence band dependent on lattice displacement (see Extended Data Table 1). In addition, the calculation shows 11 meV tunnel splitting of the valence band edge at $\text{R}_{\text{h}}^{\text{h}}$ displacement, which is qualitatively in good agreement with experimentally observed avoided-crossings of intra-layer and inter-layer excitons mediated by hole tunnelling. We emphasize that these results are rather qualitative, and in reality, it depends on many factors such as inter-layer distance, outer dielectric environment etc.

-

[34] Wang, L. *et al.* One-Dimensional Electrical Contact to a Two-Dimensional Material. *Science* **342**, 614–617 (2013).

[35] Kim, K. *et al.* van der Waals Heterostructures with

High Accuracy Rotational Alignment. *Nano Letters* **16**, 1989–1995 (2016).

[36] Catellani, A., Posternak, M., Baldereschi, A. & Freeman, A. J. Bulk and surface electronic structure of hexagonal boron nitride. *Physical Review B* **36**, 6105–6111 (1987).

[37] Laturia, A., Van de Put, M. L. & Vandenberghe, W. G. Dielectric properties of hexagonal boron nitride and transition metal dichalcogenides: from monolayer to bulk. *npj 2D Materials and Applications* **2**, 6 (2018).

[38] Larentis, S. *et al.* Large effective mass and interaction-enhanced Zeeman splitting of K - valley electrons in MoSe$_2$. *Physical Review B* **97**, 201407 (2018).

[39] Rytova, N. S. The screened potential of a point charge in a thin film. *Moscow University Physics Bulletin* **22**, 18 (1967).

[40] Lu, C.-P., Li, G., Watanabe, K., Taniguchi, T. & Andrei, E. Y. MoS$_2$: Choice Substrate for Accessing and Tuning the Electronic Properties of Graphene. *Physical Review Letters* **113**, 156804 (2014).

[41] He, K., Poole, C., Mak, K. F. & Shan, J. Experimental Demonstration of Continuous Electronic Structure Tuning via Strain in Atomically Thin MoS$_2$. *Nano Letters* **13**, 2931–2936 (2013).

[42] Conley, H. J. *et al.* Bandgap Engineering of Strained Monolayer and Bilayer MoS$_2$. *Nano Letters* **13**, 3626–3630 (2013).

[43] Zhu, C. R. *et al.* Strain tuning of optical emission energy and polarization in monolayer and bilayer MoS$_2$. *Physical Review B* **88**, 121301 (2013).

[44] Frisenda, R. *et al.* Biaxial strain tuning of the optical properties of single-layer transition metal dichalcogenides. *npj 2D Materials and Applications* **1**, 10 (2017).

[45] Giannozzi, P. *et al.* QUANTUM ESPRESSO: a modular and open-source software project for quantum simulations of materials. *Journal of Physics: Condensed Matter* **21**, 395502 (2009).

[46] Corso, A. D. Pseudopotentials periodic table: From H to Pu. *Computational Materials Science* **95**, 337–350 (2014).

[47] Rasmussen, F. A. & Thygesen, K. S. Computational 2D Materials Database: Electronic Structure of Transition-Metal Dichalcogenides and Oxides. *The Journal of Physical Chemistry C* **119**, 13169–13183 (2015).

[48] Zollner, K., Faria Junior, P. E. & Fabian, J. Proximity exchange effects in MoSe$_2$ and WSe$_2$ heterostructures with CrI$_3$: Twist angle, layer, and gate dependence. *Physical Review B* **100**, 085128 (2019).

DATA AVAILABILITY

The data that support the findings of this study are available in the ETH Research Collection (http://hdl.handle.net/20.500.11850/399579).
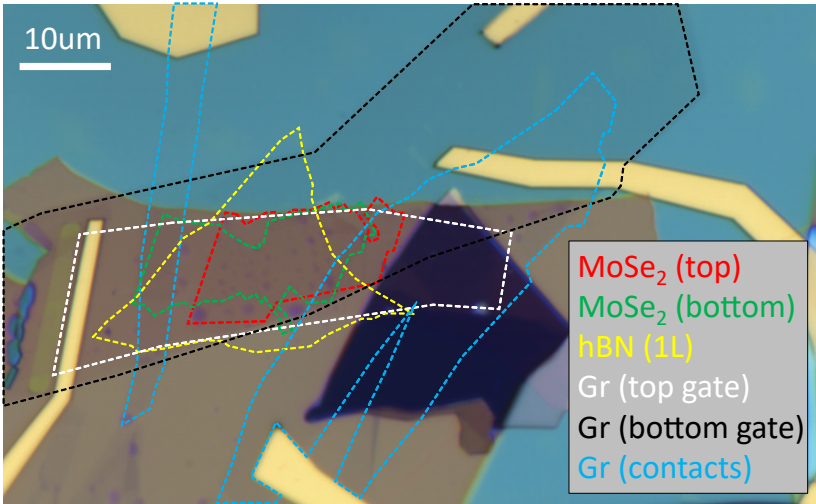
Extended Data Figure 1 — Optical microscope image of the device. The border of each flake is highlighted with dashed lines, and the material is indicated in the gray box with the corresponding color. (The abbreviation "Gr" stands for Graphene.)
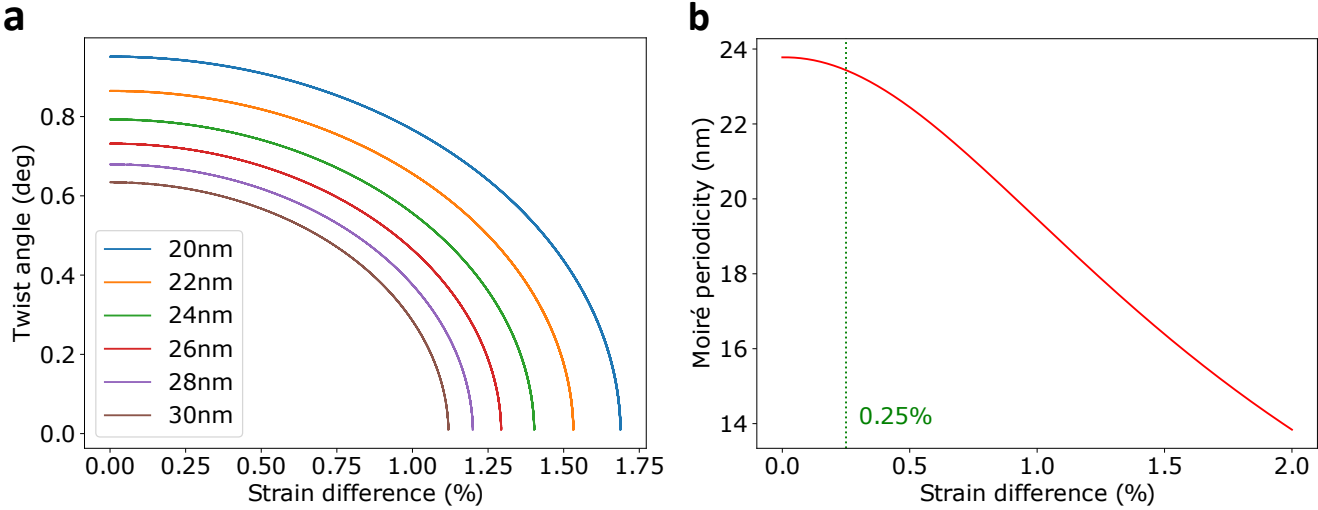
Extended Data Figure 2 — Effect of twist angle and strain on moiré periodicity. a Plot of the relation between twist angle and strain difference which gives same moiré periodicity ($\lambda_{\mathrm{moiré}}$), shown from $\lambda_{\mathrm{moiré}} = 20\,\mathrm{nm}$ to $30\,\mathrm{nm}$. **b** Strain difference dependence of moiré periodicity for fixed twist angle $0.8°$.
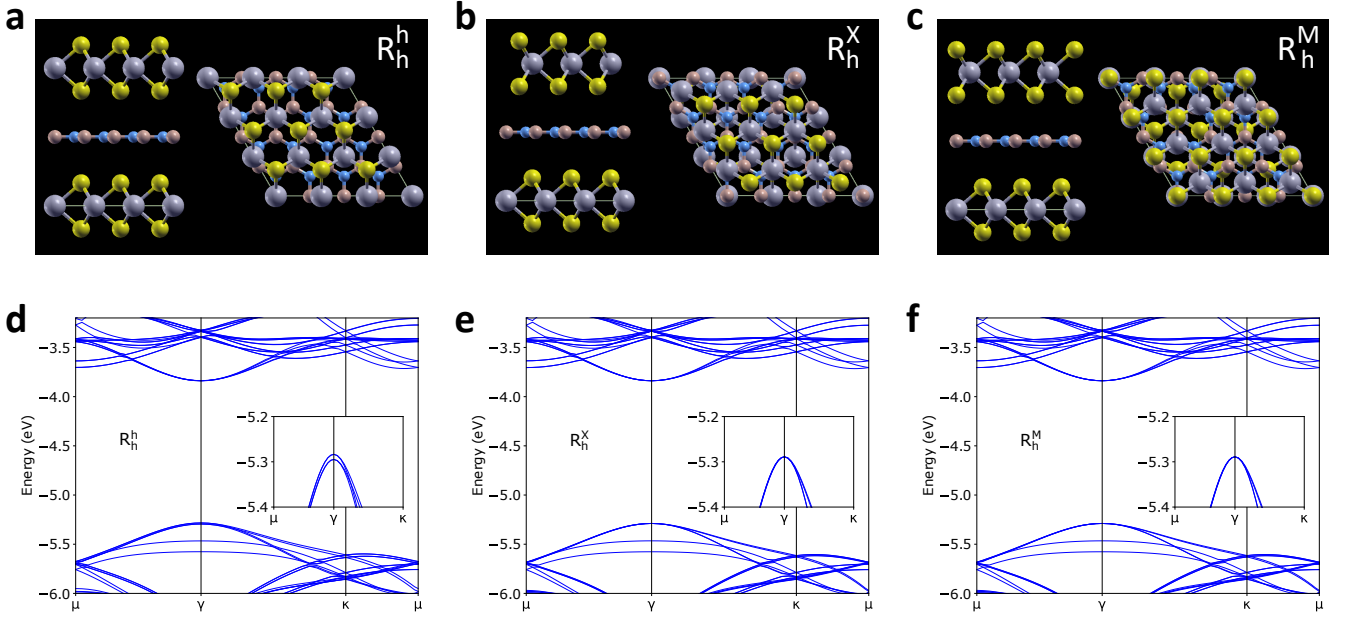
Extended Data Figure 3 — Band structure of R-stacked MoSe$_2$/hBN/MoSe$_2$ heterostructure obtained from density functional theory (DFT) calculation. **a** to **c** show the side and top view of the supercell used for the calculation. **d**, **e** and **f** show the calculated band structure of R-stacked MoSe$_2$/hBN/MoSe$_2$ for R$_h^h$, R$_h^X$ and R$_h^M$ lattice displacement, respectively. The insets show the magnified plot of the valence bands around γ point.

Lattice displacement	R$_h^h$	R$_h^X$	R$_h^M$
Lowest conduction band edge (eV)	-3.8389	-3.8383	-3.8383
Highest valence band edge (eV)	-5.2835	-5.2889	-5.2890

Extended Data Table 1 — DFT calculation results of MoSe$_2$/hBN/MoSe$_2$